ARTICLE

Microstructurally Engineered Nanocrystalline Fe-Sn-Sb Anode: Towards Stable High Energy Density Sodium-ion Batteries

Received 00th January 20xx,
Accepted 00th January 20xx

DOI: 10.1039/x0xx00000x

Eldho Edison,[a] Sivaramapanicker Sreejith,*[b] Hao Ren,[a] Chwee Teck Lim *[b,c] and Srinivasan Madhavi *[a]

To facilitate the commercialization of sodium-ion batteries (SIB's), advanced electrode materials with high sodiation capacities and enhanced cycling stabilities are essential. Herein, we investigate the effect of Fe incorporation into SnSb to generate a new ternary nanocrystalline composite based anode which improves the cycling stability and performance of SIB's. We ensure a high-throughput synthetic approach via rapid-solidification technique for efficient and industrially viable Fe-Sn-Sb alloy synthesis. Interestingly, the new ternary system possesses nanocrystalline domains that helped to alleviate the stresses induced upon the sodiation/desodiation reactions and thereby enhanced the performance. The Fe1.0-SnSb anode delivered a capacity of ~500 mAh g-1 at a specific current of 50 mA g-1 for over 120 cycles and a full-cell was designed which could deliver one of the highest reported energy densities of ~826 Wh kg-1anode. The promising electrochemical results assert the significance of microstructural engineering of alloying anodes and open up new avenues of research into rapidly solidified alloys for energy storage applications.

Introduction

Sodium-ion batteries (SIBs) are proposed as low-cost alternatives to the conventional lithium-ion batteries (LIBs) in large scale applications including grid storage.[1-4] This is not only due to the abundant and cheap sodium reserves but also the similar electrochemistry of SIBs to the LIBs.[5, 6] As a result, great efforts have been put forth to develop materials with good sodium storage performance. Various metal oxides, transition metal dichalcogenides and alloys have been explored as anodes for SIBs.[7-12] However, the tedious synthetic protocols and the huge capacity losses arising from the irreversible conversion reactions are major challenges hindering their commercialization.

Among others, Sn and Sb are of interest as they offer high gravimetric and volumetric capacities in addition to their low cost.[13, 14] While Sn can alloy with Na to form $Na_{15}Sn_4$ with a theoretical capacity of 847 mAh g^{-1}, Sb forms Na_3Sb to give 660 mAh g^{-1}.[15, 16] However, bare Sn and Sb suffer from poor cycling stability as a result of the huge volume changes associated with the sodiation/desodiation reactions. Various strategies have been employed to tackle the issue of poor cycling stability in this class of alloying anodes. More often, strategies including use of intermetallics, alloy/carbon composites, engineering the morphology of active materials and tuning the binder/electrolyte were employed for enhancing alloy anode performance.[17, 18]

Notably, SnSb alloy synergizes on the high sodiation capacities of both Sn and Sb. However, it has been discovered that the sequentially occurring alloying reactions of Sb and Sn leads to huge volume changes and rapid capacity fading.[19, 20] Hence, various groups have investigated the SnSb anode for SIBs in the recent past. For instance, Qin *et al.* developed SnSb/graphene composite to buffer the volume changes and impart cycling stability to the anode.[21] Choi *et al.* introduced chemical etching of SnSb alloy to form porous structure which could enhance the cycling stability of the anode.[22] Other approaches include SnSb nanocrystals, SnSb/carbon nanofiber composites which aid in enhancing the cycling stability.[23-25]

Herein, we report a new strategy via incorporation of guest component on SnSb matrix to get a ternary Fe-Sn-Sb alloy. Synthesis of this three-component intermetallic system was achieved via scalable and cost-effective rapid solidification technique, envisaging an enhanced cycling stability over pure SnSb anode. We found that the rapid solidification process aided the formation of nanocrystalline domains which mitigated the stresses induced upon sodiation/desodiaiton reactions. Among others, the $Fe_{1.0}$-SnSb alloy anode delivered

[a] School of Materials Science and Engineering, Nanyang Technological University, 50 Nanyang Avenue, 639798, Singapore. Email: madhavi@ntu.edu.sg
[b] Biomedical Institute for Global Health Research and Technology, National University of Singapore, 117599, Singapore. Email: ssreejith@nus.edu.sg ; sreejith.siva@gmail.com
[c] Department of Biomedical Engineering, National University of Singapore, 2 Engineering Drive 3, 117581, Singapore. Email: ctlim@nus.edu.sg
† Footnotes relating to the title and/or authors should appear here.
Electronic Supplementary Information (ESI) available: [details of any supplementary information available should be included here]. See DOI: 10.1039/x0xx00000x

ARTICLE

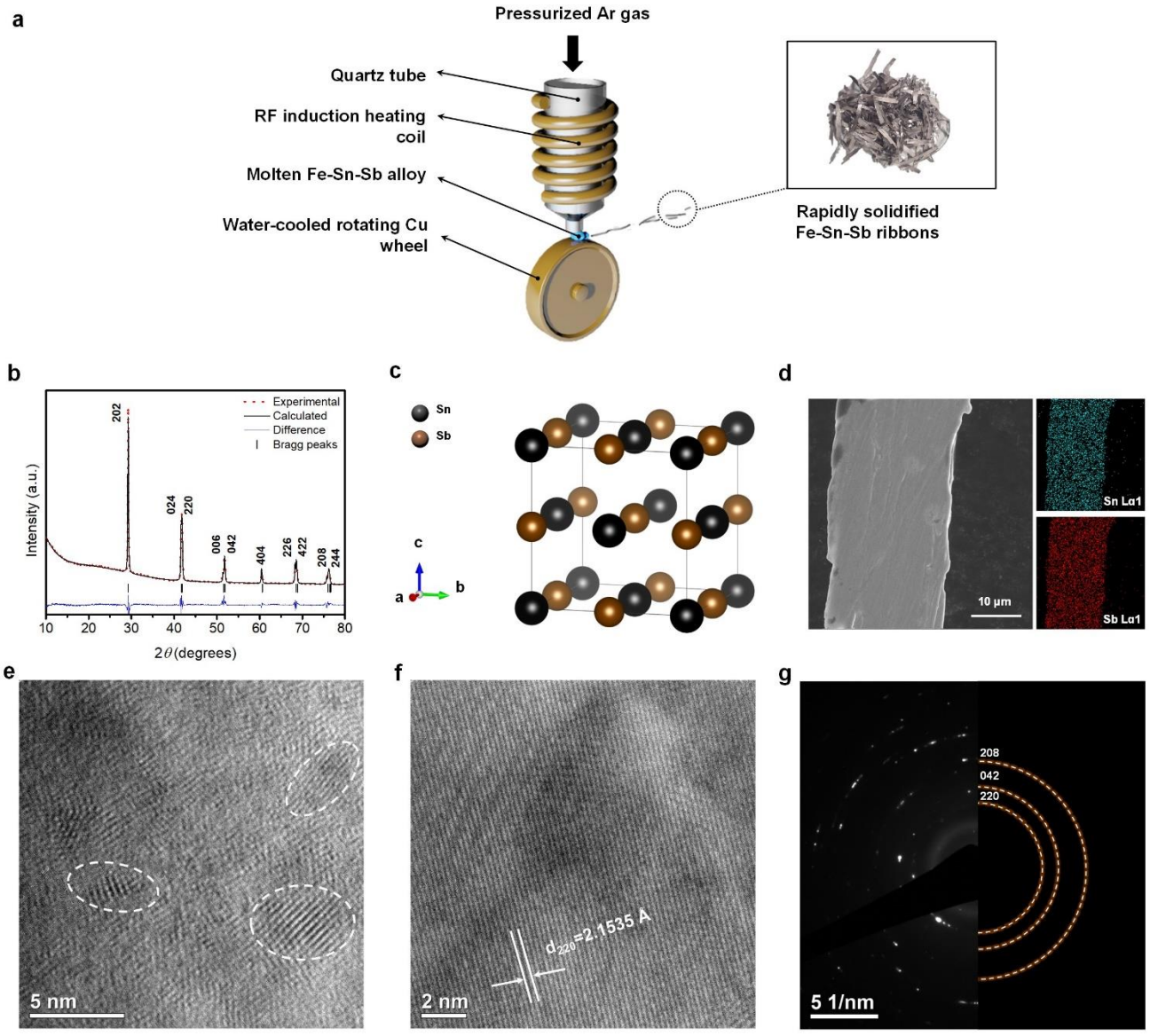

Figure 1. Rapidly solidified alloys. **a,** Schematic diagram showing the rapid-solidification process and the alloy ribbons. **b,** Rietveld-refined XRD of SnSb ribbons obtained via rapid solidification. **c,** Crystal structure of SnSb. **d,** FESEM and EDX of the SnSb ribbon. **e-f,** HRTEM images showing nanocrystalline domains in amorphous matrix. **g**, SAED pattern of SnSb ribbons.

sodiation capacity of ~ 500 mAh g^{-1} for over 120 cycles at a specific current of 50 mA g^{-1} and a capacity of ~200 mAh g^{-1} at a high specific current of 2 A g^{-1}. The ternary anode was also employed in a full-cell configuration and attained a capacity of ~290 mAh g^{-1}_{anode} at an average voltage of 2.85 V with over 99% coulombic efficiency. The results exemplify the importance of engineering the microstructure of alloying anodes as well as the significance of employing high-throughput, industrially viable rapid solidification technique for the development of high-capacity alloying anodes for energy storage applications.

ARTICLE

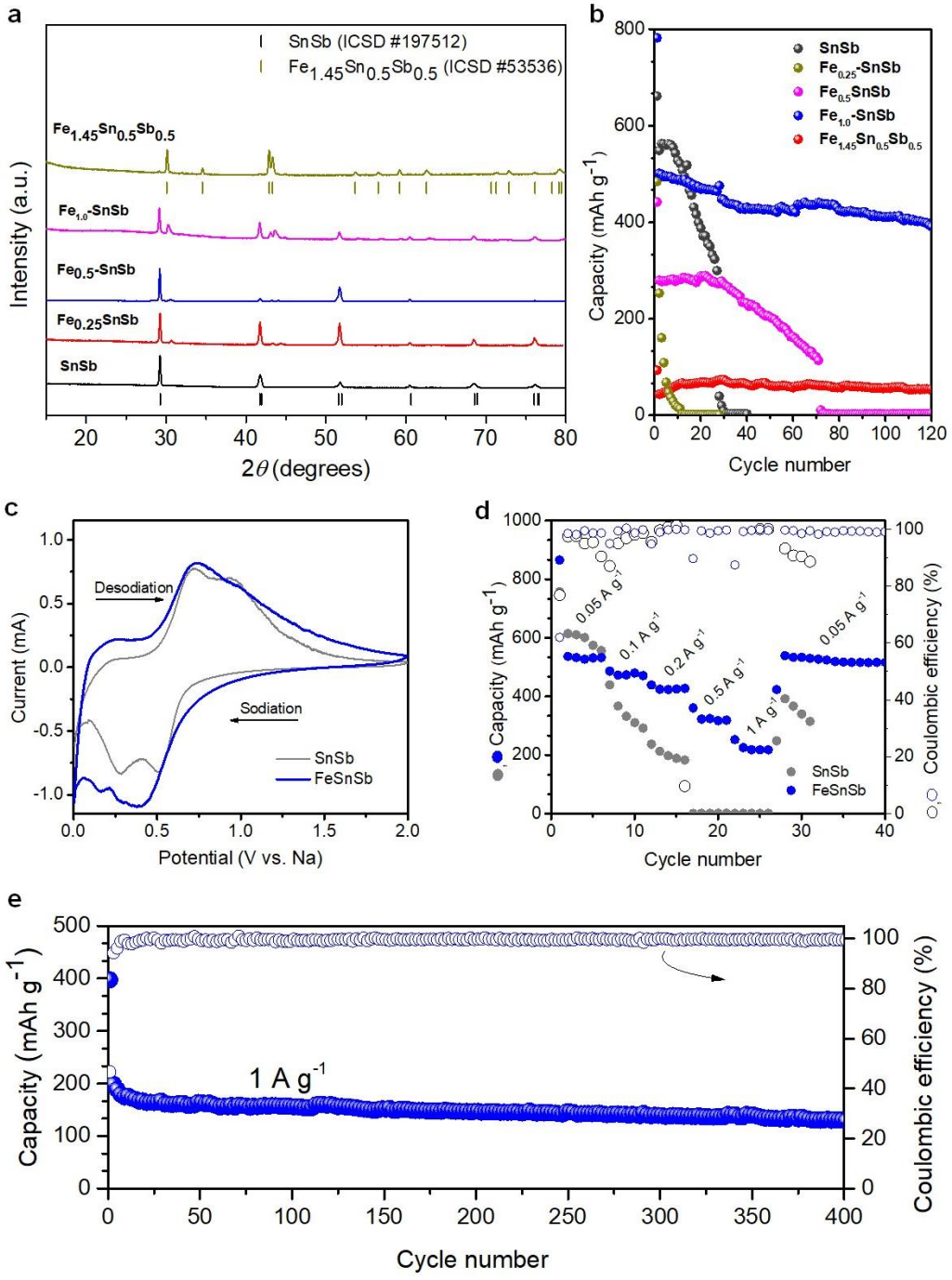

Figure 2. Rapidly solidified ternary Fe-Sn-Sb alloys. **a,** XRD patterns of the Fe-Sn-Sb alloys. **b,** Galvanostatic cycling performance of the Fe-Sn-Sb alloys at a specific current of 50 mA g^{-1} in the potential window 0.005-2 V vs Na. **c,** Cyclic voltammogram of SnSb and $Fe_{1.0}$-SnSb alloy anodes at sweep rate of 0.1 mV s^{-1}. **d,** Rate performance of SnSb and $Fe_{1.0}$-SnSb anodes. **e,** High rate cycling performance of $Fe_{1.0}$-SnSb anode at 1 A g^{-1}.

Experimental

Materials synthesis

Iron powder (99+%, Alfa-Aesar), Antimony powder (99.5%, Alfa-Aesar) and Tin powder (99+%, Alfa-Aesar) were weighed in the molar ratio and cold pressed into pellets. The Fe-Sn-Sb alloy ribbons were prepared from the pressed pellets using a single-roller melt-spinner (Edmund Bühler GmbH, Melt Spinner SC) with a 20 cm diameter Cu wheel in an argon filled chamber. The distance between the bottom of the nozzle and the surface of the copper wheel was set at 50 mm, and the rolling rate of the wheel was 50 Hz. The pellet was induction melted to molten liquid and then pressure ejected through the slotted nozzle. Upon contact with the water-cooled Copper wheel, the molten liquid rapidly solidified into very thin flakes.

Material characterization

Phase structure of the alloy ribbons was investigated by powder X-ray diffraction (XRD) (Bruker AXS, D8 Advance) using Cu K_α radiation (λ = 0.15418 nm) over 2ϑ range of 10°–80°. X-ray photoelectron spectroscopy (XPS) was carried out using Kratos AXIS Supra XPS equipped with an automated dual anode (Al/Ag Kα) X-ray monochromatic source. Field emission scanning electron microscope (FESEM) (JEOL, JSM-7600F) with energy dispersive X-ray spectroscopy (EDX) attachment and high-resolution transmission electron microscope (HR-TEM) (JEOL, JEM-2100F) were used for topological and elemental composition analysis of the melt spun flakes. For HR-TEM, the sample was first ground in mortar and pestle and dispersed in ethanol and then dripped onto copper grid and dried in vacuum oven at 60 °C.

Electrochemical characterization

The electrochemical evaluation of the materials was carried out in coin cell (CR2016) assemblies. The anodes were fabricated by mixing the Fe-Sn-Sb alloy ribbons, super-P carbon (Timcal) and carboxymethyl cellulose (Sigma-Aldrich) in the weight ratio of 8:1:1 and dispersed in de-ionized water and stirred overnight. The slurry was then cast onto a copper foil (Hohsen, Japan) and dried in air at ~60 °C for 12 h. Circular electrodes of diameter 14 mm and active material loading of ~1.5-2 mg cm^{-2} were punched out and dried further in vacuum oven at 100 °C for 12 h prior to coin cell assembly. The coin cells were then assembled in an argon-filled glovebox (MBRAUN) with moisture and oxygen content less than 1 ppm. Flattened sodium metal disk (Sigma-Aldrich) was used as the counter electrode, porous glass microfiber (Whatman Cat. No. 1825-047, UK) as the separator and a solution of 1 M $NaClO_4$ (Sigma-Aldrich) in propylene carbonate (PC, Sigma-Aldrich) and 5 vol. % fluoroethylene carbonate (FEC) as the electrolyte. Cyclic voltammetry was performed with an electrochemical workstation (Solartron 1470E) in the potential range of 0.005–2 V (*vs.* Na). The cells were cycled galvanostatically between 0.005 and 2 V (*vs.* Na) at various current densities using the NEWARE multi-channel battery test system.

Synthesis of cathode material and full-cell assembly

The cathode material, sodium vanadium fluorophosphate (NVPF) was synthesized as per a previous report.[26] Briefly, cetyltrimethylammonium bromide (CTAB, 1 mmol) was dissolved in a mixture of ethanol and deionized water (12:1). The solution was sonicated for 90 minutes. NaF (4 mmol), oxalic acid (4 mmol) and V_2O_5 (2 mmol) were added to the solution and stirred for 30 minutes. Afterwards, $NH_4H_2PO_4$ (4 mmol) was added to the solution and then stirred for 24 hours. Next, the solvent was evaporated, and the residue was ground in a mortar and pestle, followed by an annealing step in Ar at 800 °C for 5 h to obtain the $NaVPO_4F$ phase.

The electrode preparation for the cathode material is as described in section 2.3, except that aluminium foil was used for the cathode slurry coating. Prior to full-cell assembly, the $Fe_{1.0}$-SnSb anode was cycled in a half-cell assembly for two galvanostatic cycles to overcome the irreversible capacity loss in the first cycle as well as to ensure reversible capacity observed from the half-cell assembly. The cycled anode was then used for the full-cell assembly which was carried out in coin cell configuration with NVPF: $Fe_{1.0}$-SnSb active material ratio 5:1 to balance the capacity.

Results and discussions

Firstly, phase pure SnSb alloys were synthesized by rapid solidification technique following the synthesis protocol similar to our previous report.[27] Briefly, Sn and Sb metal powders (**Supporting Information Fig. S1**) were finely ground in a mortar and pestle. The well-mixed powder was then cold pressed into a pellet. The pellet was then fed into the melt-spinner through a quartz tube (**Fig. 1a**). The pellet was melted via induction heating in an Ar atmosphere. The molten liquid was then forced through the quartz tube nozzle by pressurized Ar gas, onto the surface of a water-cooled rotating copper wheel and rapidly cooled to form ribbons. As-obtained ribbons were then used as the active material in the conventional battery fabrication process.

ARTICLE

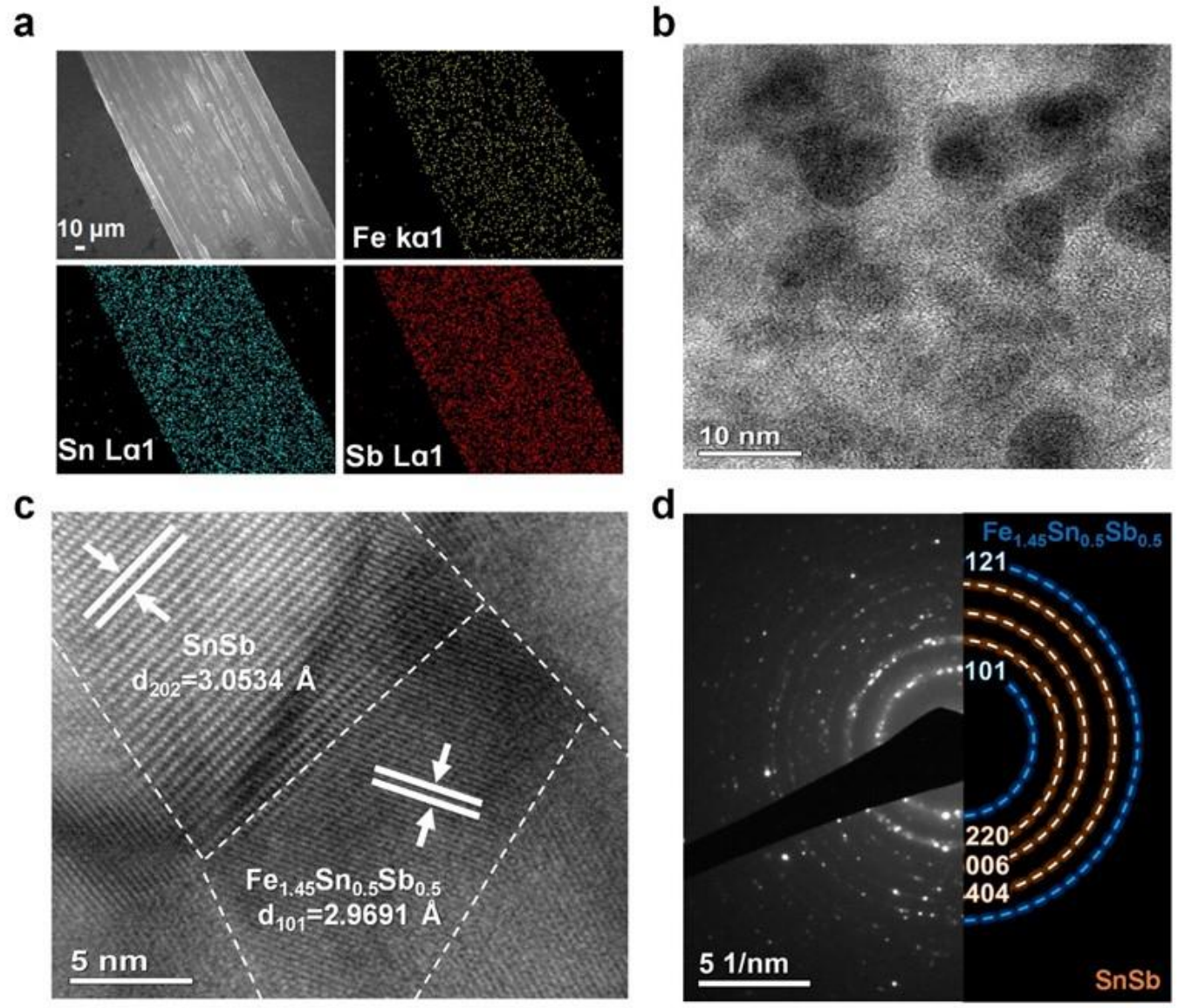

Figure 3. Morphology of $Fe_{1.0}$-SnSb alloy. **a,** FESEM and EDX revealing homogenously distributed Fe, Sn and Sb. **b-c,** HRTEM images and **d,** SAED pattern showing the nanocrystalline domains of SnSb and $Fe_{1.45}Sn_{0.5}Sb_{0.5}$ phases in the $Fe_{1.0}$-SnSb alloy.

The phase purity and crystallinity of the SnSb ribbons were attested by the Rietveld refined XRD spectra (**Fig. 1b**) which harmonized well with the trigonal crystal system in the *R-3mR* space group (ICSD #197512).[28] The lattice parameters and the refinement details are provided in the **Table S1** (**Supporting Information**). The SnSb unit cell depicted in **Fig. 1c** is identical to the NaCl structure and has alternating blocks of Sn and Sb atoms in the structure.[28] The morphology of the SnSb ribbons was investigated by FESEM and HRTEM analyses. The ribbons were nearly 20-500 microns wide (**Fig.1d, Fig. S2**) and the Sn and Sb atoms were homogenously distributed as observed from the EDX measurements (**Fig. 1d**).

A high-resolution image of ribbons revealed the nanocrystalline structure (**Fig. 1e**) attained from the rapid solidification process.[29, 30] The lattice fringes could be indexed to the *d* spacing of 2.1535 Å (**Fig. 1f**) corresponding to the (220) plane. In addition, the selected are electron diffraction (SAED) pattern (**Fig. 1g**) could also be indexed to the various lattice planes in the SnSb crystal structure. The electrochemical performance of the SnSb ribbons as sodium-ion battery anode is depicted in **Fig. S3.** The cyclic voltammogram (**Fig. S3-a**) reveals the sodiation and desodiation peaks corresponding to the following reactions:[31]

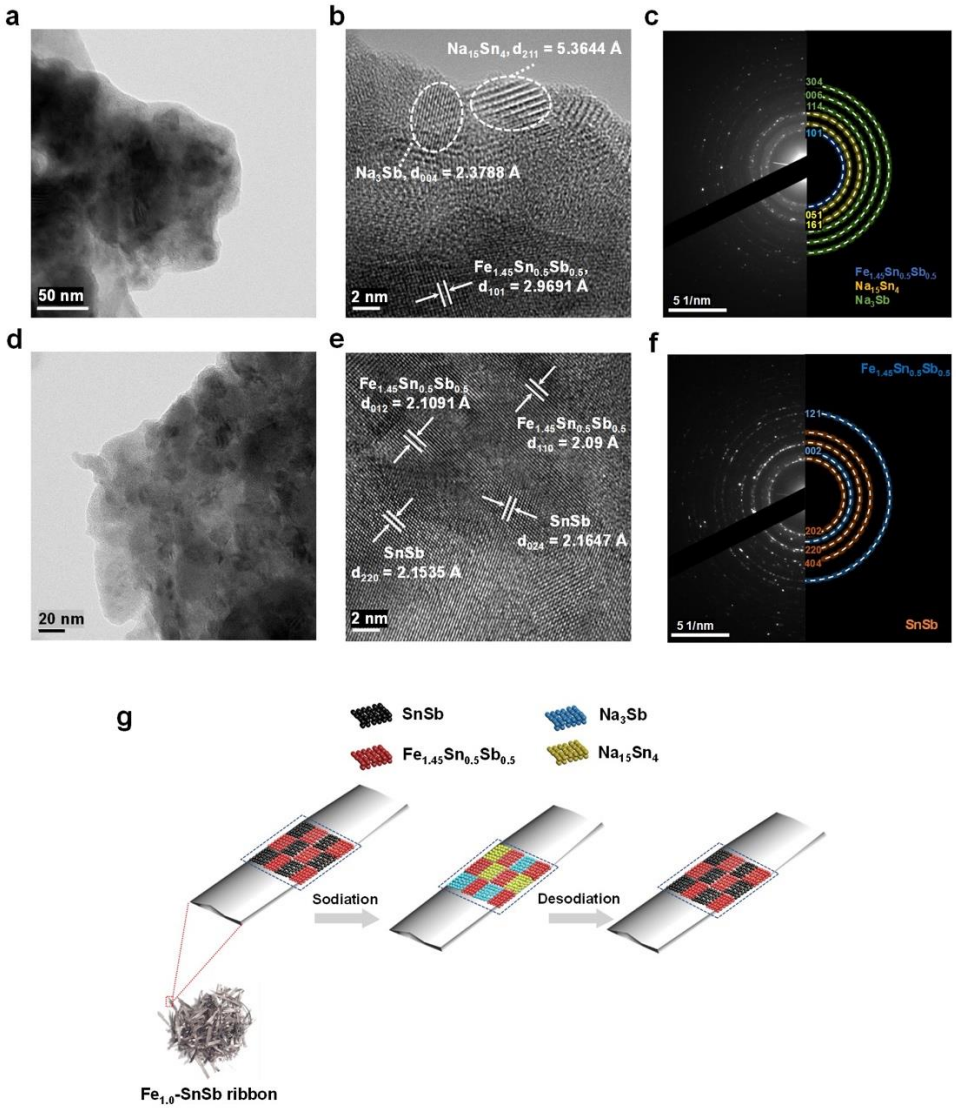

Figure 4. *Ex situ* HRTEM investigation. **a-b,** Sodiated $Fe_{1.0}$-SnSb anode. **c,** SAED pattern of sodiated $Fe_{1.0}$-SnSb anode. **d-e,** Desodiated $Fe_{1.0}$-SnSb anode. **f,** SAED pattern of desodiated $Fe_{1.0}$-SnSb anode. **g,** Schematic illustration of the sodiation/desodiation processes in $Fe_{1.0}$-SnSb alloy anode.

Sodiation:
$SnSb + 3Na \rightarrow Na_3Sb + Sn$

$Sn + xNa \rightarrow Na_xSn$

Desodiation:
$Na_xSn \rightarrow Sn + xNa$

$Na_3Sb + Sn \rightarrow 3Na + SnSb$

The galvanostatic cycling performance (**Fig. S3b**) revealed the high initial sodiation capacity close to 600 mAh g^{-1}. However, as stated above, the cycling stability was poor because of the huge volume changes occurring in the SnSb alloy during the sodiation/desodiation reactions, leading to pulverization and loss of electrical contact.[22, 31]

Next, the freshly prepared ternary Fe-Sn-Sb alloys were investigated and their galvanostatic cycling performance was studied. The various phases in the ternary system are depicted in the phase diagram (**Fig. S4**). As evident from the ternary phase diagram, the addition of Fe to SnSb would lead to multiphase fields and the ternary single phase existing is the $Fe_{1.45}Sn_{0.5}Sb_{0.5}$ phase.[32] To investigate the effect of percentage loading of guest component, we synthesized ternary alloys with various atomic percentages of Fe. The ratio of Sn and Sb were kept constant while the atomic percentage of Fe was varied from 0.25 to 1.45 to synthesize $Fe_{0.25}$-SnSb, $Fe_{0.5}$-SnSb, $Fe_{1.0}$-SnSb and $Fe_{1.45}Sn_{0.5}Sb_{0.5}$ alloys. The surface analysis of the alloys was carried out using X-ray photoelectron spectroscopy (XPS) as depicted in **Fig. S5.** Predominant metallic peaks along with weak surface oxide peaks were observed in the samples. Bulk phase purity of each ratio of Fe-Sn-Sb alloys were further analysed using XRD and found to be crystalline as evident from the XRD profiles (**Fig. 2a**). Apparently, a remarkable improvement in the galvanostatic cycling stability was observed upon increment of ratio of Fe in the ternary system (**Fig. 2b**). Upon comparing the performance of alloys with different ratios, $Fe_{1.0}$-SnSb demonstrated the best performance in terms of both capacity and cycling stability. The $Fe_{1.0}$-SnSb anode delivered a reversible capacity of nearly 500 mAh g^{-1} for over 120 cycles at a specific current of 0.05 A g^{-1}. This is one of the highest capacities achieved for SnSb-based alloying anodes reported in the recent literature (**Table S2**). While $Fe_{1.45}Sn_{0.5}Sb_{0.5}$ anode demonstrated improved cycling stability, the capacity was lower than SnSb or $Fe_{1.0}$-SnSb, due to the higher dead weight from the electrochemically inactive Fe. A comparison of the $Fe_{1.0}$-SnSb and SnSb cyclic voltammograms (**Fig. 2c and Fig. S6**) revealed a similar sodiation/desodiation profile, indicating similar alloying/dealloying reactions. The $Fe_{1.0}$-SnSb alloy anode also outperformed the SnSb anode in the rate tests carried out at different specific currents (**Fig. 2d**). This is possibly due to the lower charge transfer resistance of the $Fe_{1.0}$-SnSb anode, as observed from the impedance analysis (**Fig. S7**). In fact, the $Fe_{1.0}$-SnSb anode delivered a high capacity of nearly 200 mAh g^{-1} at a high specific current of 1 A g^{-1} (**Fig. 2e**). For comparison, we carried out galvanostatic cycling of a control sample (**Fig. S8**) consisting of physically mixed Fe, Sn and Sb powders in the same ratio and found that it is indeed the unique microstructure of the rapidly solidified $Fe_{1.0}$-SnSb alloy that aids the enhanced cycling stability as well as the excellent rate performance.

Upon investigating the morphology and microstructure, it was found that the $Fe_{1.0}$-SnSb ribbons were comprised of Fe, Sn and Sb atoms distributed as shown in **Fig. 3a**. The HRTEM images revealed nanocrystalline domains of various orientations coexisting within an amorphous matrix (**Fig. S9 and Fig. 3b, c**). Moreover, the SAED pattern (**Fig. 3d**) revealed the polycrystalline nature of the $Fe_{1.0}$-SnSb alloy. From the XRD and HRTEM analyses, the $Fe_{1.0}$-SnSb alloy was found to be a nanocomposite comprising of SnSb and $Fe_{1.45}Sn_{0.5}Sb_{0.5}$ phases existing as nanocrystalline domains (**Fig. S10, S11**). Such a unique microstructure obtained by rapid solidification could possibly explain the enhanced cycling stability of the $Fe_{1.0}$-SnSb alloy anode. Hence, we were further motivated to investigate the phase/structural changes in the $Fe_{1.0}$-SnSb anode upon sodiation/desodiation reactions.

To investigate the phase and structural evolution during the sodiation/desodiation processes, the *ex situ* HRTEM and XRD investigations of the sodiated and desodiated $Fe_{1.0}$-SnSb anode were carried out (**Fig. 4, Fig. S11**). During the sodiation process, the SnSb domains in the $Fe_{1.0}$-SnSb alloy undergoes a phase transformation to Na_3Sb and $Na_{15}Sn_4$ phases. This is observed in the HRTEM lattice fringes (**Fig. 4b**) and the indexed SAED patterns (**Fig. 4c**) as well as the *ex situ* XRD pattern of the sodiated $Fe_{1.0}$-SnSb anode (**Fig. S11**). During the desodiation process, the $Fe_{1.0}$-SnSb retains its crystalline structure and the nanocrystalline domains of SnSb and $Fe_{1.45}Sn_{0.5}Sb_{0.5}$ reappear as observed in the HRTEM and SAED pattern (**Fig. 4e, f**). Moreover, the *ex situ* XRD of the desodiated $Fe_{1.0}$-SnSb as well as the cycled $Fe_{1.0}$-SnSb anode indicated the reformation of SnSb and $Fe_{1.45}Sn_{0.5}Sb_{0.5}$ phases, suggesting the high reversibility and the structural integrity of the rapidly solidified $Fe_{1.0}$-SnSb alloy anode. This further explains the longer cycling stability of the $Fe_{1.0}$-SnSb anode when compared to the pure SnSb anode, as the $Fe_{1.45}Sn_{0.5}Sb_{0.5}$ domains present in the former could possibly mitigate the stresses and strains induced during the repeated sodiation/desodiation cycles. Hence the unique microstructure of the rapidly solidified $Fe_{1.0}$-SnSb anode helps to minimize the huge volume expansion during the sodiation/desodiation reactions and maintains the structural integrity-leading to enhanced cycling stability (**Fig. 4g**).

Motivated by the excellent half-cell performance, we investigated the electrochemical performance in a full-cell configuration by coupling with a $NaVPO_4F$ (NVPF) cathode (**Fig. 5**). The NVPF cathode was synthesized according to a previous report and delivered nearly 100 mAh g^{-1} at a specific current of 0.05 A g^{-1} with a flat voltage plateau at ~3.4 vs. Na (**Fig. S12, 5a**). The $Fe_{1.0}$-SnSb /NVPF full-cell was able to power a red LED bulb (**Fig. 5b**). The full-cell delivered ~290 mAh g^{-1}_{anode} at an average voltage of ~2.85 V corresponding to a high energy density of ~826 Wh kg^{-1}_{anode}, one of the highest reported in literature (**Table S2**).

ARTICLE

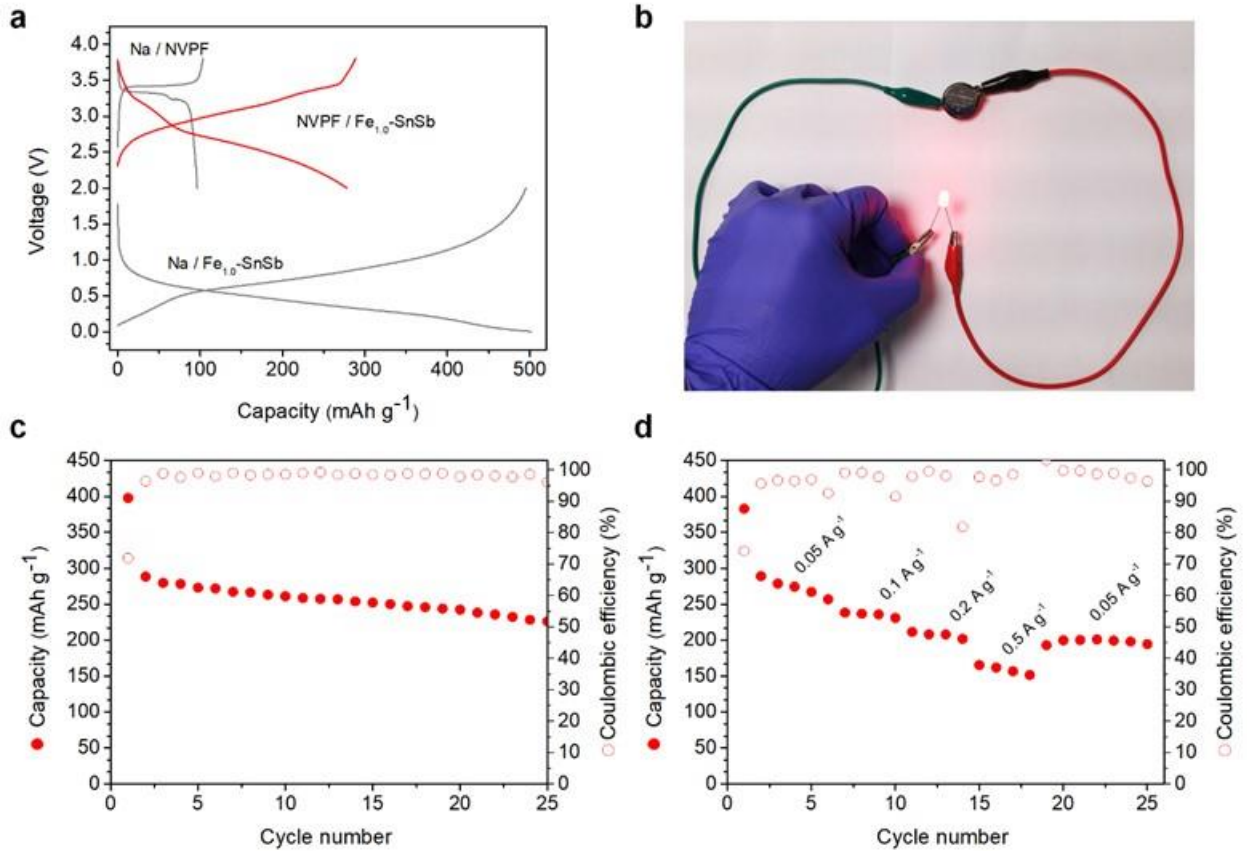

Figure 5. Full-cell performance of $Fe_{1.0}$-SnSb /NVPF couple. **a,** Potential profiles of half-cell and full-cell configurations. **b,** Red LED lamp lit by the $Fe_{1.0}$-SnSb /NVPF full-cell. **c,** Galvanostatic cycling of the full-cell at 50 mA g^{-1}. **d,** Rate performance of the full-cell.

Furthermore, the rate performance of the full-cell was also investigated and a moderate capacity of 150 mAh g-1anode was obtained at a high current rate of 0.5 A g-1. We believe that further optimizations would certainly improve the cycling and rate performances of the full-cell.

Conclusions

In conclusion, we successfully prepared a ternary Fe-Sn-Sb alloy with characteristic nanocrystalline domains using rapid solidification technique. The new ternary alloy exhibited excellent electrochemical performance as sodium-ion battery anode in both half and full-cell configurations. An unprecedented observation of the formation of nanocrystalline domains of SnSb and $Fe_{1.45}Sn_{0.5}Sb_{0.5}$, which reduces stress and strains generated during the sodiation/desodiation processes. Consequently, this phenomenon minimizes the volume changes during the sodiation/desodiation reactions, aiding excellent cycling stability. The intriguing results offer insights into the potentials of microstructural engineering of alloying anodes to enhance the energy density and cycling stability of sodium-ion batteries.

Conflicts of interest

There are no conflicts to declare.

Acknowledgements

This work was financially supported by National Research Foundation of Singapore (NRF) Investigatorship award number. NRFI2017-08/ NRF2016NRF-NRFI001-22. S. S. and C. T. L. acknowledge support from NUS-BIGHEART. We would like to acknowledge the Facility for Analysis, Characterization, Testing

and Simulation, Nanyang Technological University, Singapore, for use of their X-ray photoelectron spectroscopy, Transmission Electron Microscopy and X-ray diffraction measurements.

References

1 K. Nayak Prasant, L. Yang, W. Brehm and P. Adelhelm, *Angewandte Chemie International Edition*, 2017, **57**, 102-120.
2 N. Yabuuchi, K. Kubota, M. Dahbi and S. Komaba, *Chemical Reviews*, 2014, **114**, 11636-11682.
3 B. Dunn, H. Kamath and J.-M. Tarascon, *Science*, 2011, **334**, 928-935.
4 D. Kundu, E. Talaie, V. Duffort and L. F. Nazar *Angewandte Chemie International Edition*, 2015, **54**, 3431-3448.
5 C. Vaalma, D. Buchholz, M. Weil and S. Passerini, *Nature Reviews Materials*, 2018, **3**, 18013.
6 J. Deng, W. B. Luo, S. L. Chou, H. K. Liu and S. X. Dou, *Advanced Energy Materials*, 2017, **8**, 1701428.
7 H. Li, Y. Shi, M.-H. Chiu and L.-J. Li, *Nano Energy*, 2015, **18**, 293-305.
8 X. Ren, P. Lian, D. Xie, Y. Yang, Y. Mei, X. Huang, Z. Wang and X. Yin, *Journal of Materials Science*, 2017, **52**, 10364-10386.
9 E. Yang, H. Ji and Y. Jung, *The Journal of Physical Chemistry C*, 2015, **119**, 26374-26380.
10 M. Lao, Y. Zhang, W. Luo, Q. Yan, W. Sun and S. X. Dou, *Advanced Materials*, 2017, **29**, 1700622.
11 E. Edison, R. Satish, W. C. Ling, N. Bucher, V. Aravindan and S. Madhavi, *Journal of Power Sources*, 2017, **343**, 296-302.
12 E. Edison, W. C. Ling, V. Aravindan and S. Madhavi, *ChemElectroChem*, 2017, **4**, 1932-1936.
13 Z. Li, J. Ding and D. Mitlin, *Accounts of Chemical Research*, 2015, **48**, 1657-1665.
14 J. He, Y. Wei, T. Zhai and H. Li, *Materials Chemistry Frontiers*, 2018, **2**, 437-455.
15 J. M. Stratford, M. Mayo, P. K. Allan, O. Pecher, O. J. Borkiewicz, K. M. Wiaderek, K. W. Chapman, C. J. Pickard, A. J. Morris and C. P. Grey, *Journal of the American Chemical Society*, 2017, **139**, 7273-7286.
16 P. K. Allan, J. M. Griffin, A. Darwiche, O. J. Borkiewicz, K. M. Wiaderek, K. W. Chapman, A. J. Morris, P. J. Chupas, L. Monconduit and C. P. Grey, *Journal of the American Chemical Society*, 2016, **138**, 2352-2365.
17 M. Lao, Y. Zhang, W. Luo, Q. Yan, W. Sun and S. X. Dou, *Advanced Materials*, 2017, **29**, 1700622.
18 E. Edison, S. Sreejith, C. T. Lim and S. Madhavi, *Sustainable Energy & Fuels*, 2018, **2**, 2567-2582.
19 D. H. Youn, H. Park, K. E. Loeffler, J.-H. Kim, A. Heller and C. B. Mullins, *ChemElectroChem*, 2017, **5**, 391-396.
20 Z. Yi, Q. Han, D. Geng, Y. Wu, Y. Cheng and L. Wang, *Journal of Power Sources*, 2017, **342**, 861-871.
21 J. Qin, T. Wang, D. Liu, E. Liu, N. Zhao, C. Shi, F. He, L. Ma and C. He, *Advanced Materials*, 2018, **30**, 1704670.
22 J.-H. Choi, C.-W. Ha, H.-Y. Choi, J.-W. Seong, C.-M. Park and S.-M. Lee, *Journal of Power Sources*, 2018, **386**, 34-39.
23 M. He, M. Walter, K. V. Kravchyk, R. Erni, R. Widmer and M. V. Kovalenko, *Nanoscale*, 2015, **7**, 455-459.
24 X. Xia, Z. Li, L. Xue, Y. Qiu, C. Zhang and X. Zhang, *Journal of Materials Research*, 2017, **32**, 1184-1193.
25 H. Jia, M. Dirican, C. Chen, J. Zhu, P. Zhu, C. Yan, Y. Li, X. Dong, J. Guo and X. Zhang, *ACS Applied Materials & Interfaces*, 2018, **10**, 9696-9703.
26 M. Law and P. Balaya, *Energy Storage Materials*, 2018, **10**, 102-113.
27 E. Edison, S. Sreejith and S. Madhavi, *ACS Applied Materials & Interfaces*, 2017, **9**, 39399-39406.
28 S. Lidin, J. Christensen, K. Jansson, D. Fredrickson, R. Withers, L. Norén and S. Schmid, *Inorganic Chemistry*, 2009, **48**, 5497-5503.
29 L. Z. Zhao, W. T. Guo, Z. Y. Zhang, D. L. Jiao, J. S. Zhang, Z. W. Liu and J. M. Greneche, *Journal of Alloys and Compounds*, 2017, **715**, 60-64.
30 Y. Zhang, Y. Ji, Z. Yuan, W. Bu, Y. Qi and S. Guo, *RSC Advances*, 2018, **8**, 28969-28977.
31 W. Wang, L. Shi and Q. Li, *Journal of The Electrochemical Society*, 2018, **165**, A1455-A1459.
32 E. A. Vasilev and V. A. Virchenko, *physica status solidi (a)*, 1982, **70**, K141-K143.